Contents lists available at ScienceDirect

Applied Catalysis B: Environmental

Operando mechanistic studies of selective oxidation of glycerol to dihydroxyacetone over amorphous cobalt oxide

Truong-Giang Vo , Po-Yun Ho , Chia-Ying Chiang [*]

Department of Chemical Engineering, National Taiwan University of Science and Technology, Taipei City 10607, Taiwan

A R T I C L E   I N F O

A B S T R A C T

In this work, cobalt oxide (CoO_x) has been demonstrated as an efficient and selective electrocatalyst for producing value-added dihydroxyacetone (DHA) from industrial by-product glycerol. Under optimized conditions, DHA with high selectivity up to 45% and a high production rate of 9.6 μmol h^{-1} cm^{-2} is obtained at high current density over 3 mA cm^{-2} without the occurrence of the oxygen evolution reaction. *Operando* Raman spectroscopy features the potential-induced structural transformation between CoO_x and oxyhydroxides from which a correlation among applied potential, surface chemistry of electrocatalyst, and product distribution are built. These results point toward the viability of using inexpensive materials for electrochemical biomass upgrading as well as providing opportunities for studying structural evolution and activity origin of catalysts under realistic working conditions that can be widely extended to most electrocatalytic biomass valorization processes.

1. Introduction

Over recent years, the valorization of biomass-derived platform compounds has attracted intensive research interest as a promising and sustainable approach for the production of fine chemicals [1–3]. Glycerol, a representative polyol and a primary byproduct of the biofuel industry, is one of the most yielded products among hundreds of biomass-derived intermediates, [4] constituting an annual global supply of several million tonnes [2,5]. A large surplus increase of yearly produced glycerol compared to its demand result in it being widely available at a relatively low market price (0.24–0.6 USD/ kg) [6–8]. Therefore, notable efforts have been recently devoted to discovering new applications of glycerol as a low-cost platform molecule for producing highly valuable chemicals such as mesoxalic acid [9], or glyceric acid (GLCA) [10,11], and dihydroxyacetone (DHA). DHA is one of the most commercially beneficial value-added products (150 USD/ kg) [12, 13] among the various products of glycerol oxidation. It can be used as a sunless tanning agent by the cosmetics industry [14] or as a precursor for the synthesis of various fine chemicals [15] and biodegradable polymers [16,17]. Although several selective oxidation methods, including microbial fermentation and chemical oxidation [18], are being developed for DHA production, these processes still involve some disadvantages, such as high production cost, long operation times, and harsh conditions required for production [19]. For instance, Hirasawa

and co-workers have reported the production of DHA with a selectivity of 82% over Pd–Ag catalyst at 80 °C under an elevated oxygenated atmosphere [20]. Similarly, despite a high selectivity towards DHA has also been achieved using a homogeneous catalyst of palladium complex. This method, in particular, necessitates the use of a regulated harmful organic solvent, such as dimethyl sulfoxide or CH_3CN [21]. As a result, electrochemical oxidation method, which can be effectively conducted under benign conditions without the need of strong and toxic chemical oxidants [7], has proliferated as a viable alternative approach to other conventional methods. Additionally, beneficial cathodic hydrogen evolution or CO_2 reduction can be conveniently paired with the anodic biomass valorization, thereby increasing the economic feasibility of the overall process [7]. Importantly, this method provides unique opportunities for tuning selectivity toward certain target products by optimizing catalyst structures and regulating the applied potential, pH, or composition of the electrolyte [22]. However, regardless of these advantages, electrochemical biomass valorization remains in its infancy; and there is yet plenty of space to develop efficient and selective electrocatalysts to produce for the targeted substances. Most studies on glycerol electrooxidation so far have centered on noble metals and their alloys, such as Pt [23], Au [24], Pd [25], PtRu [26], PtSb[27], or PdAu [28], However, their scarce natural distribution, sluggish glycerol oxidation kinetics, and easy-to-poison nature by some in-situ generated carbonaceous intermediate species, limit their large-scale practical

---

* Corresponding author.
    E-mail address: cychiang@mail.ntust.edu.tw (C.-Y. Chiang).

applications [29,30]. Furthermore, it is also worth noting that the majority of glycerol electrooxidation research that has been reported was conducted at very low current densities; thus, the yield of certain products was low [10]. In this context, scientists have been directing increasing efforts toward the development of cost-effective and selectivity catalysts with satisfying activity for electrochemical glycerol valorization. Among the developed catalytically active electrocatalysts, cobalt-based oxides have received special attention as promising materials for industrial development, owing to their wide variety of sources, relative economic viability, and good chemical stability [31–33]. Importantly, cobalt oxides typically possess high activity toward various electrochemical reactions because of their abundant and diverse d-orbitals, which allow more dynamic and highly active electrons to be reactive [34,35]. In addition, owing to their rich redox chemistry, cobalt oxides can exist in a variety of oxidation states, which is advantageous for rapid redox charge transfer [32]. Regrettably, despite their potential as viable and cost-effective alternatives to expensive noble metals for use in electrocatalytic biomass conversion, Co-based oxides remain relatively underexplored.

On the other hand, due to the complexity of glycerol electrooxidation reaction (GEOR) and the diversity of oxidized products, the relationships among product distribution, reaction conditions, and the surface species of electrocatalysts must be tracked, regulated, and, where possible, correlated [36]. Therefore, *operando* experimental studies are particularly needed to forecast the GEOR mechanism and catalytic active sites on these metal oxides' surfaces. Unfortunately, such mechanistic knowledge of this reaction in an electrochemical context is not well-developed and *operando* studies are even rarer. Considering all the aforementioned issues, we employed a simple and controllable photochemical metal-organic decomposition method to synthesize amorphous cobalt oxides for electrocatalytic glycerol oxidation. Amorphous oxides were the chosen model to explore the structure-activity relationships, considering that they could offer a larger number of randomly oriented bonds and surface-exposed defects than their crystalline counterpart, which facilitates the adsorption of the reactants onto the catalyst surface [37,38]. By performing *operando* Raman spectroelectrochemical measurements, we were able to obtain insights into the GEOR process, establish a rigorous structure-activity-selectivity relationship, and

propose a tentative reaction pathway.

2. Experimental section

2.1. Catalyst preparation

The amorphous CoO_x thin film was deposited on fluorine-doped tin oxide (FTO) substrate by photochemical metal-organic decomposition method [39] and is schematically shown in Fig. 1(a). Briefly, the precursor was prepared by dissolving cobalt (II) 2-ethylhexanoate (65 wt%, Sigma Aldrich) in n-hexane (95%, Sigma Aldrich), following by sonication for 3 min 35 μL of the precursor was dropped on FTO substrate and spin-coated at 2500 rpm for 8 s. Afterwards, the as-coated film was placed under a ultraviolet lamp (λ = 254 nm, UVGL-58, USA) for 36 h, and followed by heating for 1 h at 100 °C to eliminate the organic ligands in the samples.

2.2. Physicochemical characterizations

The morphology of the samples was carried out by the field emission scanning electron microscope (FESEM, JSM-6500 F) and transmission electron microscopy (TEM, FEI Tecnai G2 F30). The crystalline structure was investigated by X-ray diffraction (XRD, D8 Bruker, Germany) using a monochromatic Cu Kα radiation (λ = 0.15405 nm) at a scan rate of $0.1° \, s^{-1}$. The chemical valence state and electronic properties of the surface of the film were studied by an X-ray photoelectron spectroscopy (XPS, VG ESCALAB 250). The C 1s binding energy of 284.8 eV was taken as the reference binding energy for charge correction.

2.3. Electrocatalytic activity evaluation

Electrochemical measurements were conducted with an Autolab potentiostat (PGSTAT204, Netherlands), using a conventional three-electrode configuration at room temperature (Fig. S1). The working electrode was as-prepared catalysts ($1 \, cm^2$) while the counter electrode was a Pt mesh (25 mm × 25 mm) and the reference electrode was an Ag/AgCl (in 3 M KCl). The electrolyte was containing 0.1 M glycerol in 0.1 M $Na_2B_4O_7$ solution (pH = 9) unless otherwise specified. The
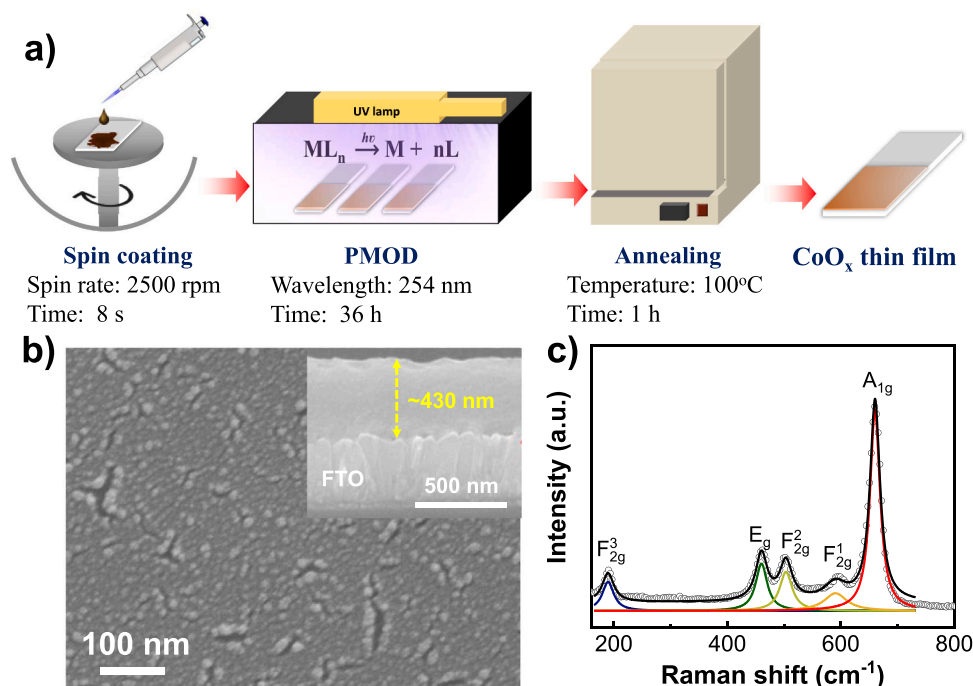

Fig. 1. (a) Schematic illustration outlining the CoO_x preparation process; (b) surface and cross-sectional SEM images of CoO_x; c) Raman spectra of CoO_x film.

$Na_2B_4O_7$ electrolyte was chosen to lower the pH away from the strong basic condition, so the consumption of DHA and production of formic acid can be supressed [40,41]. To study the reaction pathway by the electrochemical oxidation of GEOR products, 5 mM of the respective molecule such as glyceraldehyde (GLYD), dihydroxyacetone (DHA), glyceric acid (GLCA), or formic acid (FA) was added to 0.1 M $Na_2B_4O_7$ aqueous solution. Before current-potential (J-V) measurement, the CoO_x electrode was subjected to continuous voltammetry cycling at 50 mV s^{-1} until stable current responses were obtained. A freshly-prepared electrolyte solution was used in all electrochemical measurements to ensure the reproducibility of the results. All the potentials were reported versus reversible hydrogen electrode (RHE) by using the following equation,

$$V_{RHE} = V_{Ag/AgCl} + 0.21 + 0.0591 \text{ pH} \tag{1}$$

where V_{RHE} is the potential versus RHE, pH is the pH of the electrolyte solution, and $V_{Ag/AgCl}$ is the potential against Ag/AgCl reference electrode.

GEOR was carried out at different constant potentials of 1.5, 1.7, and 1.9 V_{RHE} under gently stirring. High-performance liquid chromatography (HPLC, Young Lin YL-9100, Korea) equipped with a photodiode array detector and ion-exclusion column (RCM-Monosaccharide Ca^{+2}, Phenomenex) was used to separate and quantify the products from the glycerol oxidation. The eluent was a 0.5 mM aqueous solution of H_2SO_4 with a constant flow rate of 0.5 mL/min and the column temperature was set at 70 °C. Aliquots of the reaction mixture (200 μL) were withdrawn at hourly intervals for high-performance liquid chromatography (HPLC) analysis. The injection volume was fixed at 25 μL for all samples. The selectivity was calculated as a percentage of all products, with the amount of each product divided by the total amount of all products. A gas chromatograph equipped with a thermal conductivity detector (GC, Young Lin YL-6500GC) was also employed to analyze the gaseous products during the GEOR process. The carrier gas (argon) was used at a flow rate of 12 mL/min. The injector, column and detector temperatures were set at 180 °C, 40 °C and 180 °C, respectively.

2.4. Operando Raman spectroscopy

Operando Raman studies were performed with a confocal micro-Raman spectrometer (MRID, Protrustech, Taiwan) with a 532 nm laser as excitation source. A home-build acrylic electrochemical cell, which features the same CoO_x working electrode and reference electrode, but a Pt wire electrode was used. The same potentiostat (Autolab, PGSTAT204, Netherlands) was utilized to apply external bias to the working electrode during Raman experiments. Potential-dependent Raman spectroscopy was measured either under open-circuit conditions or during potentiostatic electrolysis with different applied potentials. The Raman spectra were acquired with an acquisition time of 30 s and at × 20 accumulation, from 100 to 2000 cm^{-1}. In order to quantify the relative changes in the Raman bands, the as-obtained spectra were fitted with the Lorentzian function using Origin software (OriginLab Corporation, USA).

3. Results and discussion

3.1. Material characterization

Fig. 1(b) shows the microstructures of the CoO_x film, which were observed by SEM from the top-view for the surface morphology and the side-view for film thickness. The CoO_x film revealed a relatively dense surface morphology composed of very small grains that appeared to be evenly distributed over the FTO substrate. There were minor cracks associated with ligand cleavage and solvent evaporation during the preparation process. As shown in the cross-sectional view in the inset figure, a relatively compact layer of ca. 430 nm was observed. The

crystal structure of CoO_x film was investigated using XRD, as shown in Fig. S2 in the Supporting information (SI). The resulting spectra revealed no discernible diffraction peaks, implying that the as-deposited film was either amorphous or made up of sub-nanometer-sized crystallizes [42]. As shown in Fig. S3, the selected area electron diffraction pattern of CoO_x exhibits a broad and diffuse halo ring. Meanwhile, there is no evident crystal lattice can be found in the high-resolution TEM images. These results further confirm the amorphous features of the as-prepared film, which is in good agreement with XRD analysis.

In order to further investigate the local crystal structures of the CoO_x, *ex-situ* Raman spectroscopy was conducted under dry conditions, as seen in Fig. 1(c). A collection of five active Raman modes were distinguished in the range of 190–700 cm^{-1}. The Raman band at 190 cm^{-1} corresponded to F_{2g}^3 mode of the tetrahedral sites (CoO_4) while the band at 660 cm^{-1} can be attributed to the symmetric Co-O vibration of the octahedral (CoO_6) group. Two medium intensity Raman bands observed at 459, 503 cm^{-1} and a weak band located at 590 cm^{-1} can be assigned to the E_g, F_{2g}^2, F_{2g}^1 symmetry, respectively. These observed modes were found to be consistent with previously reported values for Co_3O_4 spinel structure [43], yet with an average shift of ca. 10 cm^{-1} attributable to size variances [44,45]. Thus, it can be assumed that the prepared cobalt oxides mainly consisted of Co_3O_4.

XPS was also used to study the surface composition and oxidation states of as-prepared CoO_x films were as shown in Fig. 2. The full-scan spectra of CoO_x verified the existence of Co, O, and C (Fig. 2a). Whereas the emergence of C 1s is supposedly triggered by the presence of ubiquitous carbon (Fig. 3b), the Co 2p and O 1s have been further analyzed, as shown in Fig. 2(c) and (d). As shown in Fig. 2(c), the Co 2p region was deconvoluted into two pairs of spin-orbit doublets and a pair of associated shake-up satellites (referred to as "sat."). Two peaks centered at 780.1 and 781.7 eV can be assigned to Co^{3+} and Co^{2+}, respectively. The O 1s species in the fine-scan XPS spectra showed the main signal at 531.7 eV, representing defects with lower oxygen coordination in the Co_3O_4 matrix and a lower binding energy signal positioned at 530.2 eV for lattice oxygen [46,47].

3.2. Electrochemical performance of CoO_x

Fig. 3(a) shows current-potential (J-V) curves of CoO_x catalysts with or without adding 0.1 M glycerol. In the absence of glycerol, CoO_x electrodes drove the oxygen evolution reaction with the onset potential (V_{on}) around 1.6 V_{RHE} (black line in Fig. 3a). Notably, the V_{on} values of CoO_x electrocatalyst exhibited a remarkable cathodic shift to ~1.45 V_{RHE} after introducing 0.1 M glycerol into the electrolyte, suggesting the favorable GEOR kinetics over CoO_x. Interestingly, the GEOR onset potential of CoO_x was also approximately 150 mV lower than in our previous study on CuO electrocatalyst [40], which can mainly be attributed to the fact that CoO_x possesses a variety of oxidation states and diverse d-orbitals, which can facilitate the rapid redox charge transfer [32].

The influence of the applied potentials on the durability of CoO_x during GEOR was investigated by potentiostatic electrolysis at three potentials, 1.5, 1.7, and 1.9 V_{RHE}. As shown in Fig. 3(b), following an approximately 30% decrease in current density over the first hour, amorphous CoO_x maintains relatively stable current behavior for the remainder of the 3 h test. In principle, the decline of the current might have been caused by the chemical stability of the catalyst, chemisorption of reaction intermediates, or a decrease in the concentration of reactant species at the electrode surface [48]. Thus, to confirm the stability and understand the real active sites during the electro-oxidation of glycerol, after running GEOR for 3 h, morphology and crystal structure of CoO_x was re-evaluated investigated by SEM, Raman and XPS. As shown in Figs. S4a and S4b, there was no visible change in the morphology of CoO_x were observed, suggesting the electrode surface was well-maintained after running GEOR for 3 h. The high-resolution XPS

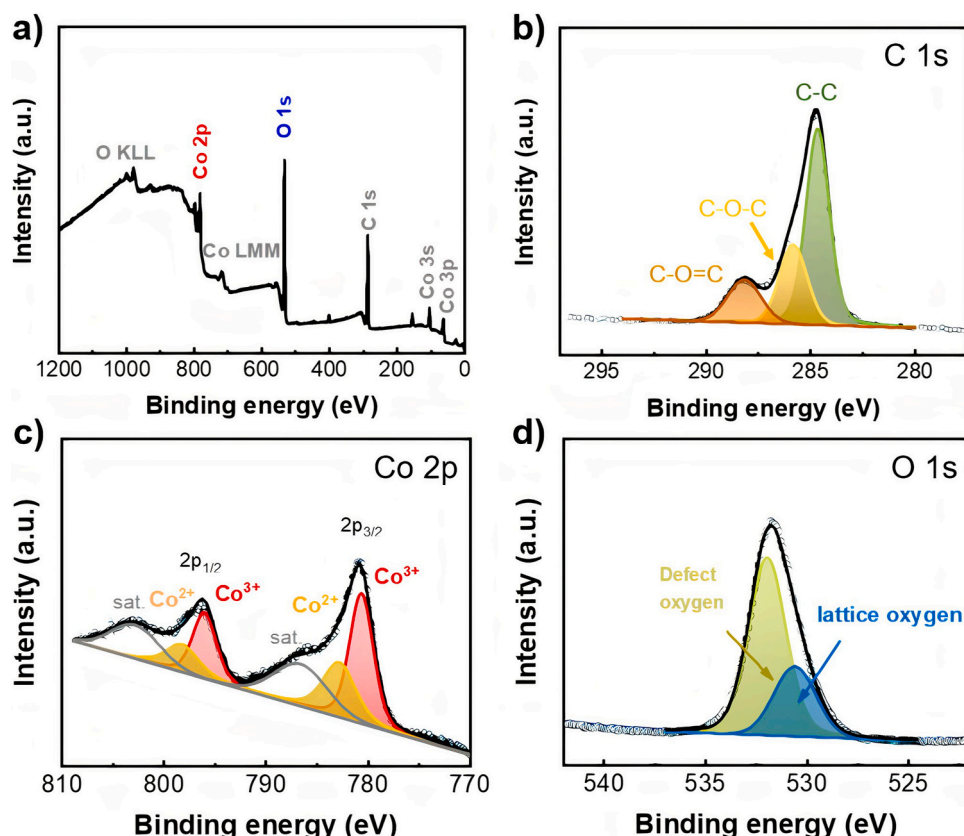**Fig. 2.** (a) the full XPS spectrum of CoO_x and the high-resolution XPS spectra of (b) C 1s, (c) Co 2p and (d) O 1s.

spectra of the CoO_x electrocatalyst after GEOR showed a mixture of Co^{2+} and Co^{3+}, which was almost identical to that of the as-synthesized one. *Ex-situ* Raman spectra show that there was a certain degree of oxyhydroxides were formed after the GEOR (Fig. S5), hinting that the high-valence cobalt species might act as the active species during the glycerol electrooxidation, which will be discussed in further section. These findings unequivocally confirm the stability under continuous working conditions of the CoO_x electrocatalyst. The current density decrease, therefore, could be ascribed to the chemisorption of reaction intermediates, which prevented fresh glycerol molecules from approaching the electrode surface, as well as the possible change in the electrolyte pH [49]. Indeed, the various acid products (GLCA and FA) generated from the glycerol oxidation could consume OH^- in the electrolyte solution, leading to a continuous decrease in the pH near the electrode surface [50], which would further reduce the GEOR reaction rate.

Considering that an ideal glycerol oxidation electrocatalyst should possess high catalytic activity without the concurrence of competitive oxygen evolution reaction, the evolved gas species during the course of GEOR were collected and quantified by means of gas chromatography (Fig. S5). It can be observed that no trace amount of oxygen was detected, indicating that the competitive oxygen evolution reaction did not occur at the anode. In addition, as shown in Fig. S6, the measured H_2 amount was well-matched with the theoretically predicted values, indicating that the Faradaic efficiency for H_2 was consistently close to 100%. Therefore, it is reasonable to rule out the possibility that oxidized products might be accumulated or be reduced at the cathode [51].

Next, the potential-dependent products of GEOR were then identified and quantified by HPLC (Fig. S7). It should be noted here that, for simplicity, although they may exist as salts in mild alkaline solution (pH 9), some of the products in the figure are denoted by their acid forms. As shown in Fig. 4, the CoO_x electrocatalyst yielded four different products, including DHA, GLYD, GLCA, and FA, depending on applied potentials.

DHA was found to be the dominant oxidized product at all investigated potentials and a maximum selectivity of 60% was obtained at 1.5 V_{RHE}. The selectivity of GLYD achieved the largest values of ca. 30% at 1.5 V_{RHE} and was less sensitive to the variance of applied potential. GLCA, which is a product of the consecutive oxidations of GLYD or DHA, was only formed in a limited amount (5–7%) at potentials greater than 1.5 V_{RHE}. Simultaneously, as the potential increased from 1.5 to 1.7 V_{RHE}, as shown in Fig. 4 and Table S1, the selectivity and Faradaic efficiency towards DHA declined marginally from 60% and 49.4 to 40% and 34.6%, respectively. Meanwhile, selectivity and Faradaic efficiency for GLYD remained the same, suggesting that GLCA more likely originated from the further oxidation of DHA. It is also discovered that the elongation of reaction time would only increase the production yield while having little influence on the product distribution. It is important to note that the remarkable DHA selectivity obtained in this work (~45–60%) is among the highest results reported in the literature thus far for noble-metal-free electrocatalysts and even favorably comparable to that of platinum-based electrocatalyst, as indicated in Table S2. For instance, Zhou and coworkers reported the selectivity toward DHA of 45% with a maximum current density of only 0.3 mA cm^{-2} with 45% to DHA over Pt/C at 0.9 V [52]. Along with DHA, CoO_x also yielded ~25% GLYD and ~10% GLCA, making the selectivity of valuable 3 C products substantially higher than other previous studies. Additionally, the potential-dependent productivities of all GEOR products are also presented in Fig. 4(d)–(f), showing that the product yields continuously increased with the increase of the external bias. Carbon balance, which reflects the difference between the amount of carbon in the feed (i.e., glycerol) and the amount of carbon in the detected products that presented in the liquid phase, was also roughly calculated by Eq. S1 and found to be less than 2% at all conditions. The observed carbon deficiency could likely result from the adsorption of products on the electrode surface.
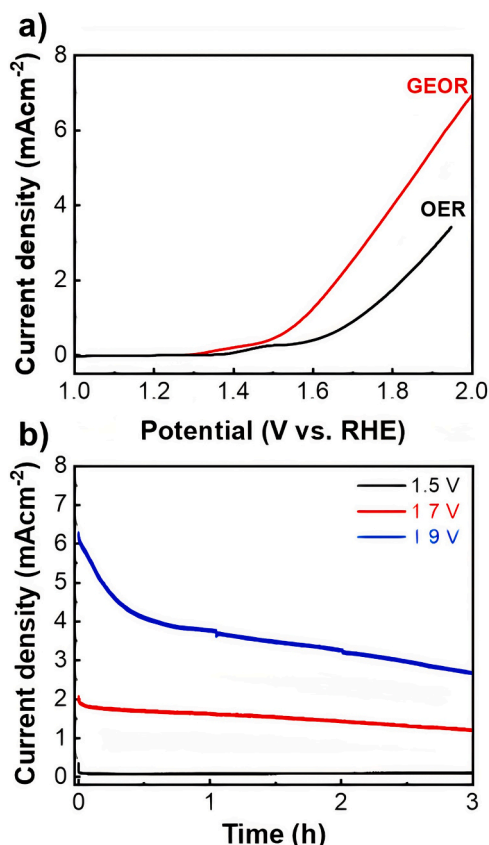
Fig. 3. (a) J-V curves for both water oxidation and glycerol oxidation; (b) J-t curves of GEOR over CoO_x at 1.5, 1.7, and 1.9 V_{RHE} in 0.1 M glycerol containing 0.1 M $Na_2B_4O_7$ solution (pH 9).

3.3. Operando Raman investigation of glycerol oxidation on CoO_x

With the aim of gaining a better mechanistic understanding of the GEOR over CoO_x, *operando* Raman spectroscopy was conducted, and the schematic illustration of the corresponding cell layout is shown in Fig. 5 (a). Various data, namely the change in catalysts' surface or the presence of reaction intermediates during the course of glycerol electrooxidation, could be collected by positioning the focus point of the laser beam toward the catalyst interface or liquid phase.

Before conducting *operando* Raman measurements, for ease of band assignment, the Raman spectra of $Na_2B_4O_7$, glycerol, and possible oxidation products were also recorded; these are shown in Fig. 5(b). When the optimized oxidation potential of 1.7 V_{RHE} was applied, the Raman spectra of the liquid phase near the CoO_x surface were first collected (illustrated in Fig. S8) while Lorentz fitting of the selected region is presented in Fig. 5(c). The change in the Raman signal correlates to the production/consumption of reaction intermediates during the GEOR. As shown in the figures, the formations of DHA (1266 cm^{-1}), GLYD (1310 cm^{-1}), and FA (1388 cm^{-1}) were observed in the first 20 min. No signal for GLCA was found during the first 40 min, suggesting that no further oxidation of DHA or GLYD occurred during the early stage of the process. As more time elapsed, the C−C−C bending of GLAD (~1310 cm^{-1}) became attenuated as the vibration bands from GLCA appeared at 1240 and 1340 cm^{-1}. No identifiable band from glycolic acid (1710 cm^{-1}), an intermediate product from the overoxidation of GLCA, was detected. These observations demonstrated the GLCA was likely originated from the subsequent oxidation of DHA, and the reaction came to a halt at the formation of GLCA, rather than progressing to the undesirable C2 or C1 products. Furthermore, considering that FA was observed consistently during the whole process even where GLCA had not yet formed, the presence of FA at the beginning of the test was

likely caused by the C−C cleavage of glycerol. Thus, the Raman spectra provide strong supplementary evidence that supports the hypothesis derived from HPLC.

Following the identification of reaction intermediates, we turned out attention to understanding the dynamic surface chemistry of CoO_x during the GEOR. Fig. 6(a)–(c) displayed *operando* Raman spectra of CoO_x electrodes which were held at successively more positive from open-circuit potential to 1.7 V_{RHE}. Aside from the characteristic bands of spinel Co_3O_4 mentioned in the previous section, the Raman spectra recorded at open-circuit potential (the lowermost black line) featured a new ubiquitous peak located at 515 cm^{-1}, which is characteristic of Co$(OH)_2$. When moderately positive potential (1.2 V_{RHE}) was applied (as in Fig. 6a), the attenuation of Co_3O_4 bands was accompanied by the rise of a broad band centered at ~580 cm^{-1}, indicating the conversion of surface oxides into (oxy)hydroxide [53,54]. This change occurred within a 10 min time frame after applying an anodic potential. Further spectral changes were visibly observed with the prolongation of reaction time: the broad feature located at ca. 580 cm^{-1} grew in intensity while the most intense peak at 680 cm^{-1} continuously decreased but did not fade completely. Considering that the presence of broad vibrational bands may arise from the in-situ transformation of surface oxides into amorphous (oxy)hydroxide, these broad bands were fitted using Lorentzian functions for further quantitative analysis. Fitted spectra are presented in the righthand panels of Fig. 6, whereas peak positions and assignments are summarized and presented in Table 1. As anodic potentials were increased from 1.2 to 1.7 V_{RHE}, progressive oxidation of CoO_x/Co$(OH)_2$ to CoOOH was observed. The A_{1g} mode (~680 cm^{-1}) and the E_g (460 cm^{-1}) modes of Co_3O_4, as well as the characteristic peak of Co$(OH)_2$ (514 cm^{-1}), were further attenuated. Simultaneously, three broad CoOOH peaks at 369, 578, and 612 cm^{-1} and one peak from CoO_2 (474 cm^{-1}) increased in intensity. The higher the applied potential, the faster the transformation rate, as a result, the greater oxyhydroxide content. It should be noted that the positions of certain bands in the present study vary slightly from those recorded in previous reports. This disparity may be due to the existence of many disorders and defects in amorphous CoO_x material [55]. At high potentials, owing to the formation of Co^{3+}/Co^{4+} with strong oxidation ability as dominant components, the CoO_x electrocatalyst was capable to oxidize both -OH and -C=O groups, generated DHA and GLCA.

3.4. Proposed mechanism of GEOR on the CoO_x electrocatalyst

Given that the GEOR glycerol can take place in several parallel routes with a variety of potential intermediate products, the examination of the electrochemical oxidation of individual GEOR intermediate products can deepen understanding of the GEOR process. As such, electrochemical oxidation of DHA, GLYD, GLCA, or FA over CoO_x was also carried out under conditions identical to those used for glycerol oxidation. The typical voltammetric profiles for the oxidation of reaction products in 0.1 M $Na_2B_4O_7$ solution are shown in Fig. S9. Comparing the voltammetric profiles of product oxidation with that of glycerol oxidation, a coincidence can be seen in the oxidation features in the range of 1.0–1.9 V_{RHE}. The oxidation products were analyzed by HPLC shown in Fig. S10. The oxidation of both GLYD and DHA produced GLCA as the only products, implying that the oxidation of glycerol began with the formation of GLYD and DHA as primary products, which were then further oxidized to GLCA. In the meantime, only FA was observed as GLCA was oxidized. As stated in the previous section, FA was observed as the oxidation product from 1.5 V_{RHE} when GLCA formation was detected (1.7 V_{RHE}). We, therefore, postulated that FA species detected at low potentials are produced mostly from the glycerol C-C bond splitting.

To this end, based on the aforementioned observations, we would like to draw up a detailed mechanistic scheme for the GEOR on the CoO_x electrocatalyst, shown in Scheme 1. First, we observed from *operando* Raman results that oxidation of glycerol likely proceeds with the
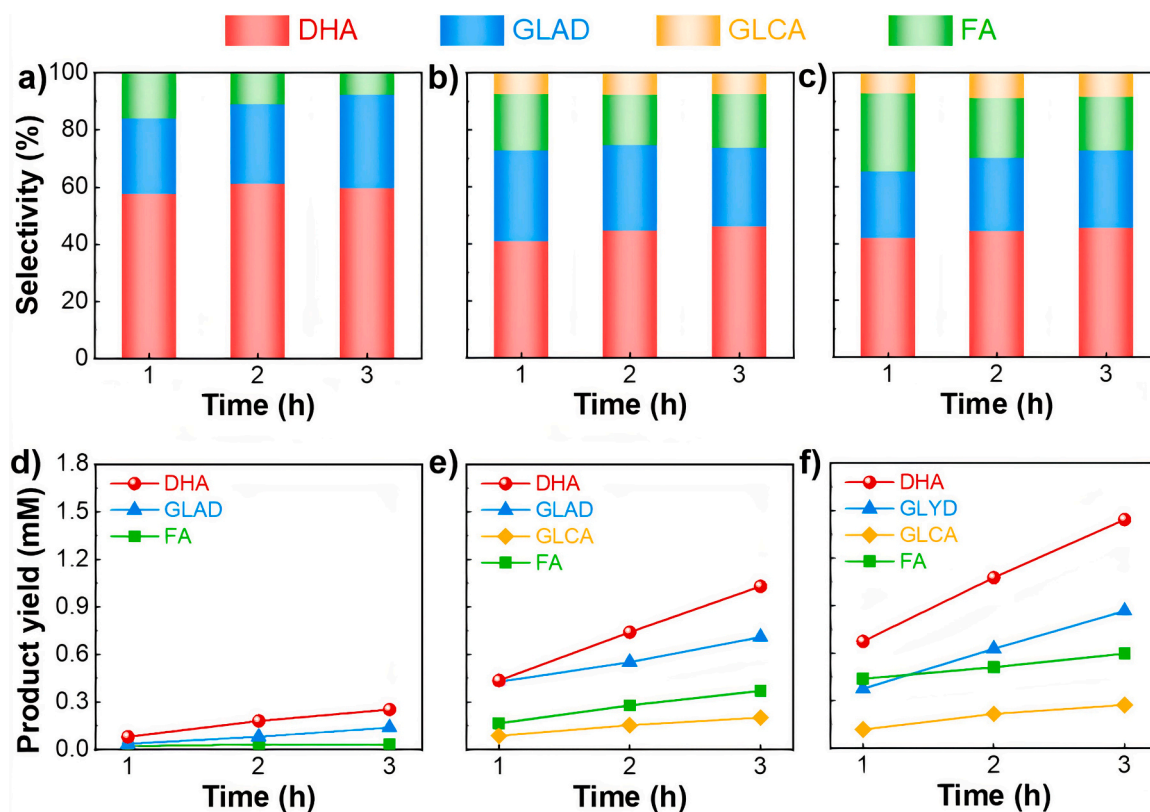
Fig. 4. Time-dependent product distribution and productivity obtained during GEOR in 0.1 M Na$_2$B$_4$O$_7$ containing 0.1 M Glycerol at different applied potentials (a, d) 1.5 V, (b, e) 1.7 V, and (c, f) 1.9 V vs. RHE.
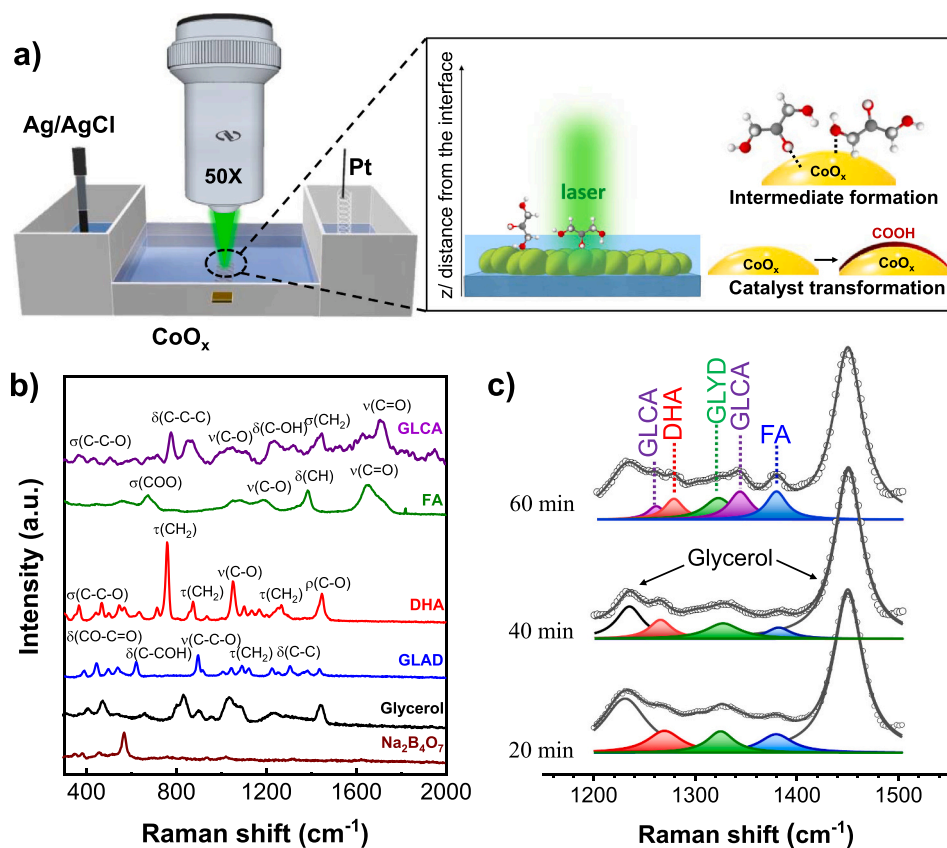
Fig. 5. (a) Schematic illustration of *operando* Raman measurement setup; (b) Raman spectra of Na$_2$B$_4$O$_7$ supporting electrolyte, glycerol, and all possible oxidation products; (c) Lorentz fitting of the time-dependent *operando* Raman spectra of GEOR collected at 1.7 V$_{RHE}$.
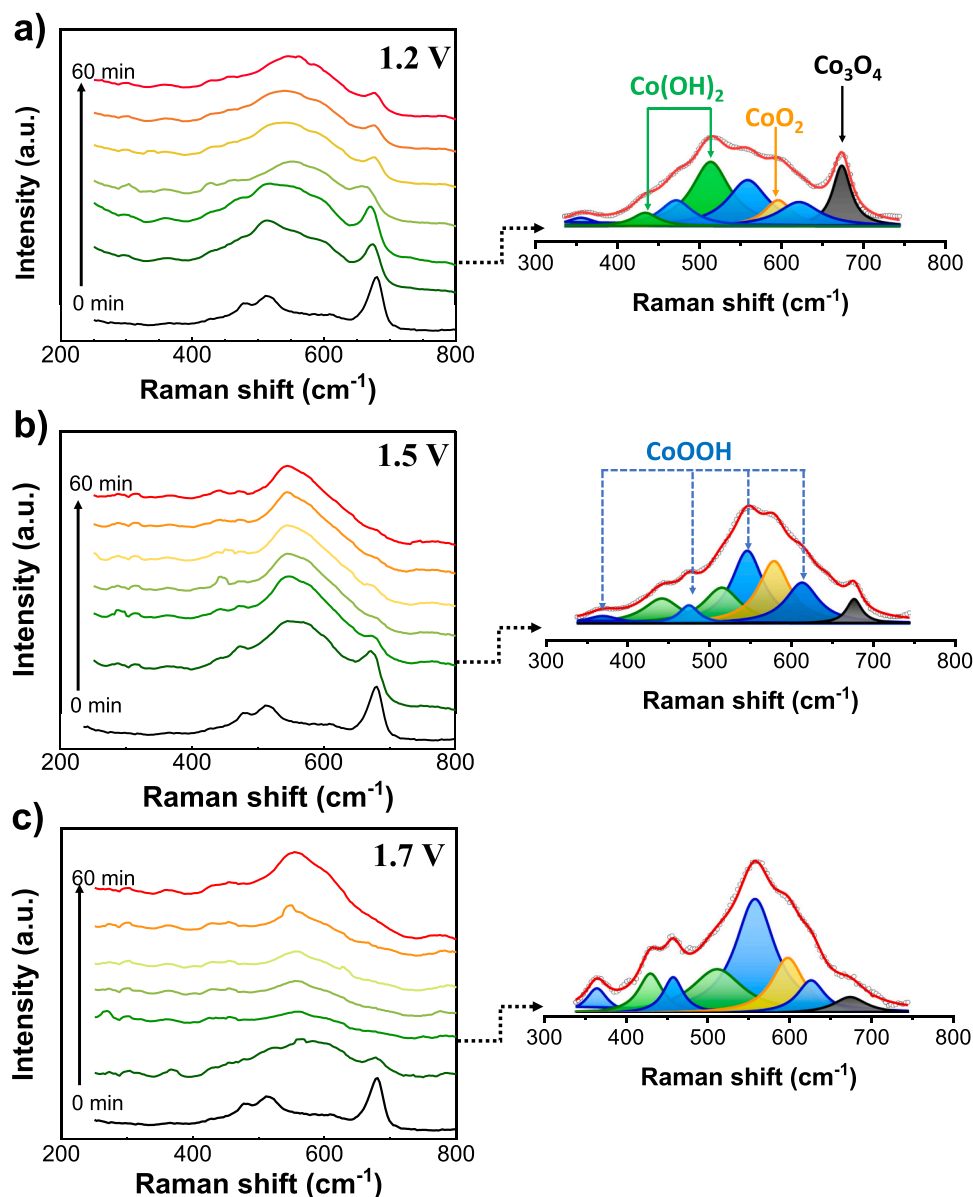
Fig. 6. Time-dependent *operando* Raman spectra of CoO$_x$ collected during GEOR at various potentials (left-panel); Lorentz fitting of *operando* Raman spectra in the selected region (right panel).

Table 1
Raman characteristic bands of cobalt-based materials.

Co$_3$O$_4$[43,53]	β-Co (OH)$_2$[55–58]	CoOOH[53]	C$_o$O$_2$[59]
194 cm^{-1} (F$_{2g}$)			
	250–285 cm^{-1} (E$_g$)	367 cm^{-1}	
481 cm^{-1} (E$_g$)	429–437 cm^{-1} (A$_{1g}$)		474–487 cm^{-1} (E$_g$)
519 cm^{-1} (F$_{2g}$)	504–523 cm^{-1} (A$_{2u}$)	503 cm^{-1}	
	598 cm^{-1} (E$_{g(R)}$)	572 cm^{-1}	581–595 cm^{-1} (A$_{1g}$)
616 cm^{-1} (F$_{2g}$)	691 cm^{-1} (E$_g$)	608 cm^{-1}	
686 cm^{-1} (A$_{1g}$)		641 cm^{-1}	

structural transformation of CoO$_x$ during the electrocatalytic oxidation of glycerol is much or less similar to what happened in oxygen evolution, as previously reported [59–61]. The starting CoO$_x$ was electrochemically oxidized and evolved into amorphous (oxy)hydroxides. Afterwards, oxyhydroxide species acted as active sites for the oxidation of glycerol or its intermediates [8]. There are two possibilities for glycerol to be oxidized, either via indirect or indirect electron transfer

mechanism. In the indirect oxidation mechanism, glycerol is oxidized to intermediate compounds and CoOOH/CoO$_2$ is reduced back to Co(OH)$_2$, leading to the depletion of CoOOH the electrode surface which is similar to the mechanism proposed by Fleischmann and co-workers for Ni-based catalyst [62]. Another possibility would be the direct mode of electron transfer in which glycerol molecules incorporate into the cobalt hydroxides surface via Langmuir-type adsorption process and are oxidized by surface OH$^-$ ions, without CoOOH consumption [62]. Considering that CoOOH is always present in significant quantities, as evidenced in *operando* Raman spectra, it is very likely that the oxidation of glycerol on CoO$_x$ proceeds via a direct oxidation pathway, although the indirect routes cannot be totally excluded. Upon adsorbing on the active sites, the GEOR may proceed via two parallel routes: (1) incomplete oxidation to C3 species through C-H breaking. This pathway begins with the initial oxidation of secondary hydroxyl groups to form DHA or primary hydroxyl ones to form GLYD. Both DHA and GLYD can be further oxidized to form GLCA and, eventually, FA; (2) direct C-C bond cleavage of glycerol leads to the production of FA [8]. In all investigated potential regions, 3 C products, namely DHA and GLYD, were found to be the
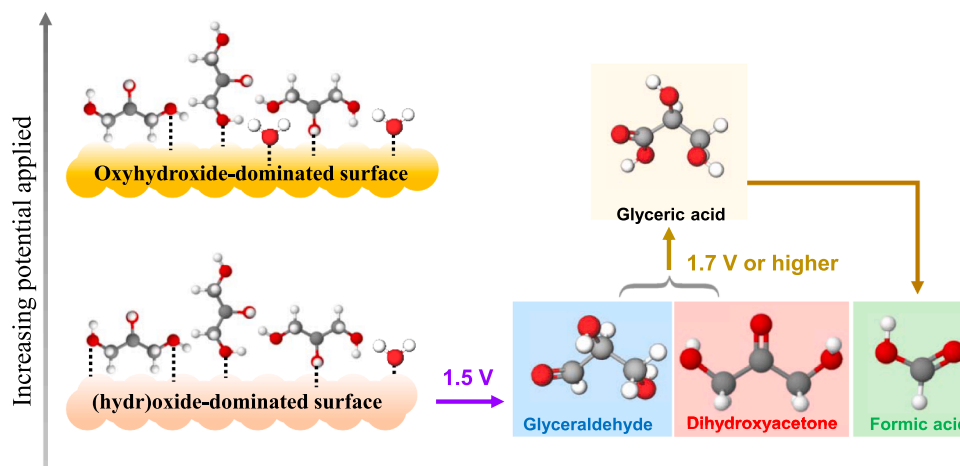
Scheme 1. Proposed GEOR pathway over CoO$_x$ electrocatalyst in mild basic media.

main products, although FA was detected in every test, indicating that C-C bond splitting may occur readily even at low applied potential (1.5 V$_{RHE}$).

4. Conclusion

In this study, we successfully demonstrated amorphous cobalt oxides as an effective and catalyst for the partial electrooxidation of glycerol to dihydroxyacetone at the anode, while simultaneously allowing H$_2$ evolution at the cathode. Importantly, we identified favorable conditions for the formation of valuable C$_3$ products, DHA and GLYD, without the need for noble-metal-based catalysts. Furthermore, with the help of *operando* Raman, we explored the potential-dependent structural changes of the cobalt redox species and reaction intermediate in the liquid phase. Thus, we propose a tentative mechanistic pathway for the selective oxidation of glycerol to C3 products in mild basic media. We hope the insights gained in this study constitute a significant step toward the understanding of the electrocatalytic transformation of glycerol and introduce a new methodology to unravel active sites under realistic working conditions that can be widely extended to most electrocatalytic biomass valorization processes.

CRediT authorship contribution statement

Truong-Giang Vo: Conceptualization, Methodology, Writing – original draft, Writing – review & editing. **Po-Yun Ho:** Methodology, Investigation. **Chia-Ying Chiang:** Supervision, Resources, Funding acquisition, Writing – review & editing, Project administration.

Declaration of Competing Interest

The authors declare that they have no known competing financial interests or personal relationships that could have appeared to influence the work reported in this paper.

Appendix A. Supporting information

Supplementary data associated with this article can be found in the online version at doi:10.1016/j.apcatb.2021.120723.

References

[1] Y. Kwon, K.J.P. Schouten, J.C. van der Waal, E. de Jong, M.T.M. Koper, Electrocatalytic conversion of furanic compounds, ACS Catal. 6 (2016) 6704–6717.

[2] L. Du, Y. Shao, J. Sun, G. Yin, C. Du, Y. Wang, Electrocatalytic valorisation of biomass derived chemicals, Catal. Sci. Technol. 8 (2018) 3216–3232.

[3] M. Simões, S. Baranton, C. Coutanceau, Electrochemical valorisation of glycerol, ChemSusChem 5 (2012) 2106–2124.

[4] T. Werpy, G. Petersen, Top. Value Added Chem. Biomass-.-.: Vol. I - Results Screen. Potential Candidates Sugars Synth. Gas., 2004 doi: 10.2172/15008859.

[5] F. Yang, J. Ye, Q. Yuan, X. Yang, Z. Xie, F. Zhao, Z. Zhou, L. Gu, X. Wang, Ultrasmall Pd-Cu-Pt trimetallic twin icosahedrons boost the electrocatalytic performance of glycerol oxidation at the operating temperature of fuel cells, Adv. Funct. Mater. 30 (2020), 1908235.

[6] R. Ciriminna, C. Della Pina, M. Rossi, M. Pagliaro, Understanding the glycerol market, Eur. J. Lipid Sci. Technol. 116 (2014) 1432–1439.

[7] X. Han, H. Sheng, C. Yu, T.W. Walker, G.W. Huber, J. Qiu, S. Jin, Electrocatalytic oxidation of glycerol to formic acid by CuCo$_2$O$_4$ spinel oxide nanostructure catalysts, ACS Catal. 10 (2020) 6741–6752.

[8] S. Feng, J. Yi, H. Miura, N. Nakatani, M. Hada, T. Shishido, Experimental and theoretical investigation of the role of bismuth in promoting the selective oxidation of glycerol over supported Pt–Bi catalyst under mild conditions, ACS Catal. 10 (2020) 6071–6083.

[9] L. Xin, Z. Zhang, Z. Wang, W. Li, Simultaneous generation of mesoxalic acid and electricity from glycerol on a gold anode catalyst in anion-exchange membrane fuel cells, ChemCatChem 4 (2012) 1105–1114.

[10] Y. Kwon, Y. Birdja, I. Spanos, P. Rodriguez, M.T.M. Koper, Highly selective electro-oxidation of glycerol to dihydroxyacetone on platinum in the presence of bismuth, ACS Catal. 2 (2012) 759–764.

[11] M. Pagliaro, R. Ciriminna, H. Kimura, M. Rossi, C. Della Pina, From glycerol to value-added products, Angew. Chem. Int. Ed. 46 (2007) 4434–4440.

[12] B. Katryniok, H. Kimura, E. Skrzyńska, J.-S. Girardon, P. Fongarland, M. Capron, R. Ducoulombier, N. Mimura, S. Paul, F. Dumeignil, Selective catalytic oxidation of glycerol: perspectives for high value chemicals, Green Chem. 13 (2011) 1960–1979.

[13] C.-Y.C. Lu-Wei Huang, Truong-Giang Vo, Converting glycerol aqueous solution to hydrogen energy and dihydroxyacetone by the BiVO$_4$ photoelectrochemical cell, Electrochim. Acta 322 (2019), 134725.

[14] R. Ciriminna, A. Fidalgo, L.M. Ilharco, M. Pagliaro, Dihydroxyacetone: an updated insight into an important bioproduct, ChemistryOpen 7 (2018) 233–236.

[15] X. Wang, F. Liang, C. Huang, Y. Li, B. Chen, Siliceous tin phosphates as effective bifunctional catalysts for selective conversion of dihydroxyacetone to lactic acid, Catal. Sci. Technol. 6 (2016) 6551–6560.

[16] M. Helou, J.-M. Brusson, J.-F. Carpentier, S.M. Guillaume, Functionalized polycarbonates from dihydroxyacetone: insights into the immortal ring-opening polymerization of 2,2-dimethoxytrimethylene carbonate, Polym. Chem. 2 (2011) 2789–2795.

[17] F.H. Isikgor, C.R. Becer, Lignocellulosic biomass: a sustainable platform for the production of bio-based chemicals and polymers, Polym. Chem. 6 (2015) 4497–4559.

[18] Y. Zhang, N. Zhang, Z.-R. Tang, Y.-J. Xu, Identification of Bi$_2$WO$_6$ as a highly selective visible-light photocatalyst toward oxidation of glycerol to dihydroxyacetone in water, Chem. Sci. 4 (2013) 1820–1824.

[19] D. Hekmat, R. Bauer, V. Neff, Optimization of the microbial synthesis of dihydroxyacetone in a semi-continuous repeated-fed-batch process by in situ immobilization of Gluconobacter oxydans, Process Biochem. 42 (2007) 71–76.

[20] S. Hirasawa, H. Watanabe, T. Kizuka, Y. Nakagawa, K. Tomishige, Performance, structure and mechanism of Pd–Ag alloy catalyst for selective oxidation of glycerol to dihydroxyacetone, J. Catal. 300 (2013) 205–216.

[21] R.M. Painter, D.M. Pearson, R.M. Waymouth, Selective catalytic oxidation of glycerol to dihydroxyacetone, Angew. Chem. Int. Ed. 49 (2010) 9456–9459.

[22] Y. Zhou, Y. Shen, J. Piao, Sustainable conversion of glycerol into value-added chemicals by selective electro-oxidation on Pt-based catalysts, ChemElectroChem 5 (2018) 1636–1643.

[23] Z. Zhang, L. Xin, W. Li, Electrocatalytic oxidation of glycerol on Pt/C in anion-exchange membrane fuel cell: cogeneration of electricity and valuable chemicals, Appl. Catal. B Environ. 119–120 (2012) 40–48.

[24] J. Qi, L. Xin, D.J. Chadderdon, Y. Qiu, Y. Jiang, N. Benipal, C. Liang, W. Li, Electrocatalytic selective oxidation of glycerol to tartronate on Au/C anode catalysts in anion exchange membrane fuel cells with electricity cogeneration, Appl. Catal. B Environ. 154–155 (2014) 360–368.

[25] M. Simões, S. Baranton, C. Coutanceau, Electro-oxidation of glycerol at Pd based nano-catalysts for an application in alkaline fuel cells for chemicals and energy cogeneration, Appl. Catal. B Environ. 93 (2010) 354–362.

[26] H.J. Kim, S.M. Choi, M.H. Seo, S. Green, G.W. Huber, W.B. Kim, Efficient electrooxidation of biomass-derived glycerol over a graphene-supported PtRu electrocatalyst, Electrochem. Commun. 13 (2011) 890–893.

[27] S. Lee, H.J. Kim, E.J. Lim, Y. Kim, Y. Noh, G.W. Huber, W.B. Kim, Highly selective transformation of glycerol to dihydroxyacetone without using oxidants by a PtSb/C-catalyzed electrooxidation process, Green Chem. 18 (2016) 2877–2887.

[28] M. Mougenot, A. Caillard, M. Simoes, S. Baranton, C. Coutanceau, P. Brault, PdAu/C catalysts prepared by plasma sputtering for the electro-oxidation of glycerol, Appl. Catal. B Environ. 107 (2011) 372–379.

[29] M.E. Ghaith, G.A. El-Nagar, M.G. Abd El-Moghny, H.H. Alalawy, M.E. El-Shakre, M.S. El-Deab, Electrocatalysis by design: enhanced electro-oxidation of glycerol at NiOx nanoparticle modified 3D porous carbon felts, Int. J. Hydrog. Energy 45 (2020) 9658–9668.

[30] A. Ashok, A. Kumar, J. Ponraj, S.A. Mansour, F. Tarlochan, Single step synthesis of porous NiCoO2 for effective electrooxidation of glycerol in alkaline medium, J. Electrochem. Soc. 165 (2018) J3301–J3309.

[31] Y. Haldorai, S.R. Choe, Y.S. Huh, Y.-K. Han, Metal-organic framework derived nanoporous carbon/Co3O4 composite electrode as a sensing platform for the determination of glucose and high-performance supercapacitor, Carbon 127 (2018) 366–373.

[32] D. Khalafallah, O.Y. Alothman, H. Fouad, K. Abdelrazek Khalil, Hierarchical Co3O4 decorated PPy nanocasting core-shell nanospheres as a high performance electrocatalysts for methanol oxidation, Int. J. Hydrog. Energy 43 (2018) 2742–2753.

[33] S. Mondal, R. Madhuri, P.K. Sharma, Probing the shape-specific electrochemical properties of cobalt oxide nanostructures for their application as selective and sensitive non-enzymatic glucose sensors, J. Mater. Chem. C 5 (2017) 6497–6505.

[34] Z. Yin, K. Allado, A.T. Sheardy, Z. Ji, D. Arvapalli, M. Liu, P. He, X. Zeng, J. Wei, Mingled MnO2 and Co3O4 binary nanostructures on well-aligned electrospun carbon nanofibers for nonenzymatic glucose oxidation and sensing, Cryst. Growth Des. 21 (2021) 1527–1539.

[35] S. Du, Z. Ren, J. Zhang, J. Wu, W. Xi, J. Zhu, H. Fu, Co3O4 nanocrystal ink printed on carbon fiber paper as a large-area electrode for electrochemical water splitting, Chem. Commun. 51 (2015) 8066–8069.

[36] M.S.E. Houache, E. Cossar, S. Ntais, E.A. Baranova, Electrochemical modification of nickel surfaces for efficient glycerol electrooxidation, J. Power Sources 375 (2018) 310–319.

[37] D. Chen, C.-L. Dong, Y. Zou, D. Su, Y.-C. Huang, L. Tao, S. Dou, S. Shen, S. Wang, In situ evolution of highly dispersed amorphous CoOx clusters for oxygen evolution reaction, Nanoscale 9 (2017) 11969–11975.

[38] L. Li, Q. Shao, X. Huang, Amorphous oxide nanostructures for advanced electrocatalysis, Chem. A Eur. J. 26 (2020) 3943–3960.

[39] C.W. Chen, C.Y. Chiang, Molybdenum-containing amorphous metal oxide catalysts for oxygen evolution reaction, Int. J. Hydrog. Energy 42 (2017) 29773–29780.

[40] C. Liu, M. Hirohara, T. Maekawa, R. Chang, T. Hayashi, C.-Y. Chiang, Selective electro-oxidation of glycerol to dihydroxyacetone by a non-precious electrocatalyst – CuO, Appl. Catal. B: Environ. 265 (2020) 118543.

[41] D. Liu, J.C. Liu, W. Cai, J. Ma, H. Bin Yang, H. Xiao, J. Li, Y. Xiong, Y. Huang, B. Liu, Selective photoelectrochemical oxidation of glycerol to high value-added dihydroxyacetone, Nat. Commun. 10 (2019) 1–8.

[42] M. Mathankumar, S. Anantharaj, A.K. Nandakumar, S. Kundu, B. Subramanian, Potentiostatic phase formation of β-CoOOH on pulsed laser deposited biphasic cobalt oxide thin film for enhanced oxygen evolution, J. Mater. Chem. A. 5 (2017) 23053–23066.

[43] V.G. Hadjiev, M.N. Iliev, I.V. Vergilov, The Raman spectra of Co3O4, J. Phys. C Solid State Phys. 21 (1988) L199–L201.

[44] A. Diallo, A.C. Beye, T.B. Doyle, E. Park, M. Maaza, Green synthesis of Co3O4 nanoparticles via Aspalathus linearis: physical properties, Green Chem. Lett. Rev. 8 (2015) 30–36.

[45] C. Alex, S.C. Sarma, S.C. Peter, N.S. John, Competing effect of Co^{3+} reducibility and oxygen-deficient defects toward high oxygen evolution activity in Co3O4 systems in alkaline medium, ACS Appl. Energy Mater. 3 (2020) 5439–5447.

[46] C. Han, L. Nie, X. Han, J. Zhuang, J. Zhang, Y. Rui, W. Meng, A good-performance glucose sensor fabricated via rationally designing a new cobalt–metal–organic framework precursor, New J. Chem. 44 (2020) 14896–14905.

[47] Y. Xie, Z. Zhou, N. Yang, G. Zhao, An overall reaction integrated with highly selective oxidation of 5-hydroxymethylfurfural and efficient hydrogen evolution, Adv. Funct. Mater. 31 (2021), 2102886.

[48] T. Haisch, F. Kubannek, D. Chen, Y.J. Tong, U. Krewer, Origin of the drastic current decay during potentiostatic alkaline methanol oxidation, ACS Appl. Mater. Interfaces 12 (2020) 43535–43542.

[49] Z. Ke, N. Williams, X. Yan, S. Younan, D. He, X. Song, X. Pan, X. Xiao, J. Gu, Solar-assisted co-electrolysis of glycerol and water for concurrent production of formic acid and hydrogen (In Press), J. Mater. Chem. A 9 (2021) 19975–19983, https://doi.org/10.1039/D1TA02654B.

[50] A.T. Kuhn, C.Y. Chan, pH changes at near-electrode surfaces, J. Appl. Electrochem. 13 (1983) 189–207.

[51] Y. Li, X. Wei, L. Chen, J. Shi, M. He, Nickel-molybdenum nitride nanoplate electrocatalysts for concurrent electrolytic hydrogen and formate productions, Nat. Commun. 10 (2019) 5335.

[52] Y. Zhou, Y. Shen, J. Xi, X. Luo, Selective electro-oxidation of glycerol to dihydroxyacetone by PtAg skeletons, ACS Appl. Mater. Interfaces 11 (2019) 28953–28959.

[53] J. Yang, H. Liu, W.N. Martens, R.L. Frost, Synthesis and characterization of cobalt hydroxide, cobalt oxyhydroxide, and cobalt oxide nanodiscs, J. Phys. Chem. C 114 (2010) 111–119.

[54] C. Pasquini, L. D'Amario, I. Zaharieva, H. Dau, Operando Raman spectroscopy tracks oxidation-state changes in an amorphous Co oxide material for electrocatalysis of the oxygen evolution reaction, J. Chem. Phys. 152 (2020), 194202.

[55] Y.Q. Gao, H.B. Li, G.W. Yang, Amorphous Co(OH)2 nanosheet electrocatalyst and the physical mechanism for its high activity and long-term cycle stability, J. Appl. Phys. 119 (2016), 034902.

[56] N.P. Dileep, T.V. Vineesh, P.V. Sarma, M.V. Chalil, C.S. Prasad, M.M. Shaijumon, Electrochemically exfoliated β-Co(OH)2 nanostructures for enhanced oxygen evolution electrocatalysis, ACS Appl. Energy Mater. 3 (2020) 1461–1467.

[57] J. Rahbani, N.M. Khashab, D. Patra, M. Al-Ghoul, Kinetics and mechanism of ionic intercalation/de-intercalation during the formation of α-cobalt hydroxide and its polymorphic transition to β-cobalt hydroxide: reaction–diffusion framework, J. Mater. Chem. 22 (2012) 16361–16369.

[58] C. Mockenhaupt, T. Zeiske, H.D. Lutz, Crystal structure of brucite-type cobalt hydroxide β-Co{O(H,D)}2 — neutron diffraction, IR and Raman spectroscopy, J. Mol. Struct. 443 (1998) 191–196.

[59] A. Moysiadou, S. Lee, C.-S. Hsu, H.M. Chen, X. Hu, Mechanism of oxygen evolution catalyzed by cobalt oxyhydroxide: cobalt superoxide species as a key intermediate and dioxygen release as a rate-determining step, J. Am. Chem. Soc. 142 (2020) 11901–11914.

[60] R. Li, B. Hu, T. Yu, H. Chen, Y. Wang, S. Song, Insights into correlation among surface-structure-activity of cobalt-derived pre-catalyst for oxygen evolution reaction, Adv. Sci. 7 (2020) 1902830.

[61] R. Zhang, W. Ke, S. Chen, X. Yue, Z. Hu, T. Ning, Phase evolution of vulcanized Co3O4 catalysts during oxygen evolution reaction, Appl. Surf. Sci. 546 (2021), 148819.

[62] M. Fleischmann, K. Korinek, D. Pletcher, The oxidation of organic compounds at a nickel anode in alkaline solution, J. Electroanal. Chem. Interfacial Electrochem. 31 (1971) 39–49.